Dynamic Damping in Joints: Multiscale Model Taking into Account Defects in a Nominally Plane Surface

Nicolas Peyret, Gaël Chevallier, Jean-Luc Dion

Dynamic Damping in Joints: Multiscale Model Taking into Account Defects in a Nominally Plane Surface

Nicolas Peyret*

Laboratoire QUARTZ EA7393 SUPMECA PARIS — 3 rue Fernand Hainaut — F-93407 SAINT OUEN, France
nicolas.peyret@supmeca.fr

Gael Chevallier

FEMTO-ST Institute — UBFC, CNRS-UFC-ENSMM-UTBM, 24, chemin de l'Epitaphe, F-25000 Besancon, France

Jean-Luc Dion

Laboratoire QUARTZ EA7393 SUPMECA PARIS — 3 rue Fernand Hainaut — F-93407 SAINT OUEN, France

The prediction of damping remains an important research challenge in structural dynamics. This paper deals with the energy losses caused by friction in assembled structures. From previous analytical works and experimental studies of the bending vibrations of a clamped–clamped beam with original positions of the interfaces, the objective of this work is to compute the damping of the structure taking into account the local properties of the joints. The purpose is to understand and analyze the contribution of the surface defects on the damping due to the joints based on multi-spherical contacts governed by Hertz' and Mindlin's theories. A design of experiments based on the model parameters is proposed and the final results are compared to the experimental's ones.

Keywords: Jointed structures; damping; dry friction; hysteretic damping.

1. Introduction

Estimating the damping remains a important challenge in the computation of the vibration levels of jointed-structures. Computer aided design and finite element analysis are used to predict respectively inertia and stiffness with fairly good accuracy, but damping is often badly estimated, meaning that vibration amplitudes are also wrongly predicted. Linear damping is well taken into account in simulation tools, but the Softwares to study friction-induced damping (FID) remains quite sparse,

*Corresponding author.

whereas joints, such as welded points, bolted joints or rivets, are widely used to link the parts of mechanisms and structures.

Essentially, there are two distinct dissipation mechanisms. First, damping can be caused by friction between sliding parts, see for instance Berthillier *et al.* [1998], Whiteman *et al.* [1996], Poudou [2007], Korkmaz *et al.* [1993], Dion *et al.* [2013] and Chevallier *et al.* [2003]. In this case, there is a macroscopic motion between the parts of the joint. Second, damping can be caused by the structure itself through a joint between the parts. In such case, there is no macroscopic motion between the parts. Damping is induced by micro sliding or partial sliding. This means that there are sticking zones and sliding zones between the parts. Many learned authors [Goodman and Klumpp, 1993; Beards and Williams, 1977; Pian, 1957; Ungar, 1973; Ahmadian and Jalali, 2007; Metherell and Diller, 1968; Esteban and Rogers, 2000; Goyder *et al.*, 2009; Peyret *et al.*, 2010, 2011] have designed experimental testing devices to highlight the fact that the damping value in assembled structures is much greater than the inherent damping value of the material. To measure and identify the dissipated energy during both dissipation mechanisms, total sliding and partial sliding, Dion *et al.* [2013] have proposed a specific experimental setup.

The present work starts from the idea of a previous paper, see Peyret *et al.* [2010]. In the latter, the testing device was a clamped–clamped bending beam built with three parts assembled together as shown in Fig. 1. The beam material is Steel

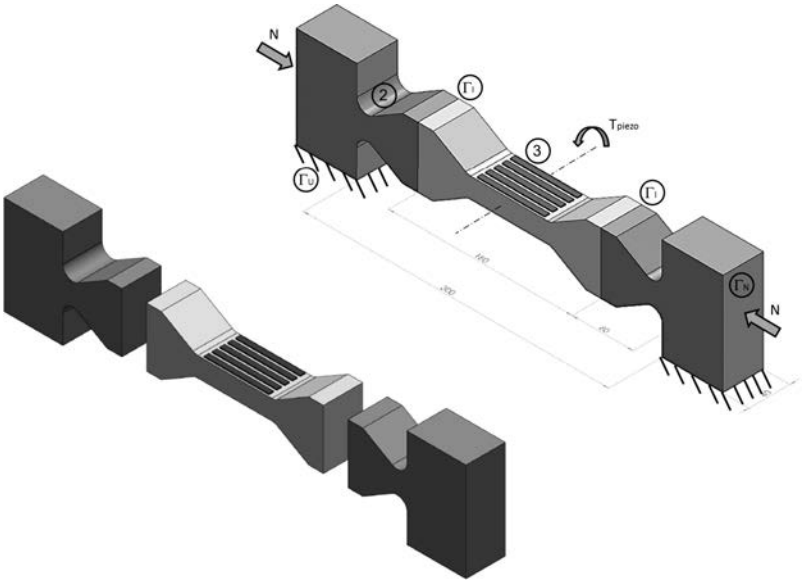

Fig. 1. View of the specimen. On the left: the three parts of the beam. On the right: the testing device assembled. Faces Γ_U are screwed on an anti-vibration marble. Strain gauges are glued on both sides (2) of the beam to measure the normal load. Piezoelectric patches (3) are glued on both sides of the beam to apply a torque T_{piezo} to excite the first vibration mode. A quick clamp is used to apply the normal load before the tests on faces Γ_N.

C35, with a Young modulus $E = 220\,\text{GPa}$ and a Poisson Coefficient $\nu = 0.3$. Cut was obtained by electrical discharge machining. The joints have been geometrically placed in order to avoid coupling between the normal load and the tangential load inside the joint, see Appendix B. In Peyret *et al.* [2009], the shape of the beam has been improved in order to obtain the greatest possible damping and to minimize the sensitivity of the results to manufacturing errors, see Fig. 1. The final design of this new testing device was presented in Dion *et al.* [2013]. The latter paper presents an original experimental procedure based on stop-sine excitation, see also Heller *et al.* [2009], obtained through piezoelectric transducers. The authors justify that their excitation method is more efficient that Dirac (shock) or Heaviside (release of a static load) excitations. Signal processing tools are proposed to post-process the instantaneous damping and frequency of the first mode. Finally, this work [Dion *et al.*, 2013] experimentally demonstrates the presence of micro-slip damping, by comparing the vibration behavior of a monolithic part and a built-up structure with friction-joints. This comparison is the best way to determine the added damping, [Segalman, 2010]. Figure 2 sums up the different results of these studies. These curves are repositioned at the intrinsic damping of the assembly (not evaluated in the models) with the goal to highlight only the damping due to the interfaces. In blue, the theoretical loss factor considering that the interface is modelled as a nominally flat surface, this result show no damping for the lower amplitudes. This result was obtained in Peyret *et al.* [2010], where the authors compute the energy losses assuming that the interfaces are perfectly plane. The modeling of the

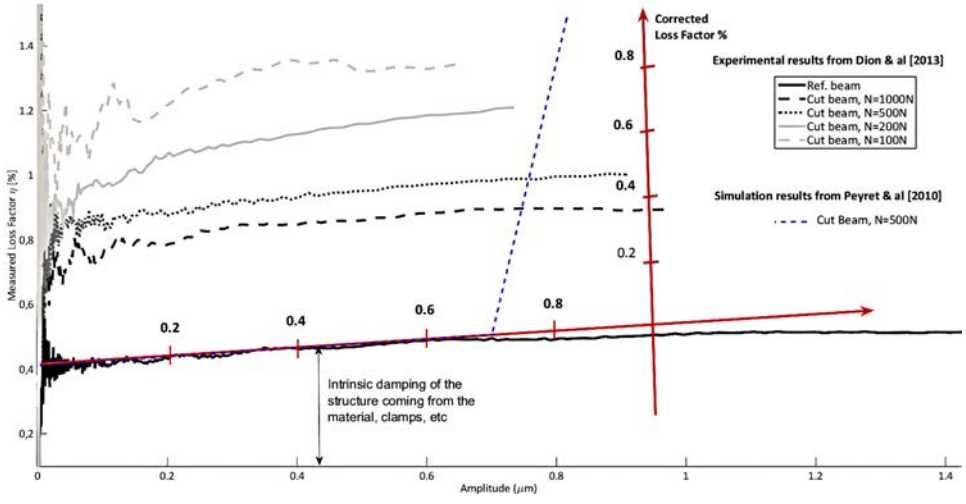

Fig. 2. Experimental results: damping versus the normal load and versus the displacement magnitude. Both the monolithic and the cut beam were tested. The latter was tested under four normal load levels in the range 100–1000 N. Simulation results: damping versus the displacement magnitude for a normal load value of 500 N.

interface by a flat surface cannot show that there are energy losses for the smallest oscillations.

To our opinion, the surface defects generated during the manufacturing process are responsible for the gap between experimental and numerical results. These defects are challenging the assumptions of flat contact interfaces and uniform normal stress fields. The contact area between both parts is geometrically defined by the nominal contact area A_0, i.e., the area where both solids seem to be in contact. In fact, because of the geometrical defects, the real contact area A_R only consists of the top surfaces of the defects. A_R is naturally smaller than the geometric surface, and the real contact pressure p_R is much higher than the nominal pressure p_0. To compute A_R and p_R, one of the most commonly used model is the Greenwood-Williamson model [Greenwood and Williamson, 1966; Greenwood and Wu, 2001]. The height and the shape of the roughness are the main parameters to compute A_R and p_R. In the Greenwood–Williamson model, the asperities are assumed to be uniformly distributed in the horizontal plane, without interaction between them, and their height is defined by a Gaussian distribution. This law seems to best match the experimental measurements and has been the subject of many mathematical developments. Moreover, the asperities are expected to have spherical ends, permitting each contact asperity to be approximated as an hertzian contact. Such models focus on real surfaces with geometrical defects of 3rd order standards [NF EN ISO 4287-4288, 1998] and [NF EN ISO 12085, 1998]. For more complexity, one can refer to: Greenwood and Tripp [1970], who took into account the roughness of different forms and other kinds of statistical distribution; Goryacheva and Dobychin [1991], who showed interactions between asperities; Tsukizoe and Hisakado [1965] and McCool [1985], who improved the uniformly distribution on the surface; Pugliese *et al.* [2008], who took into account the plasticity of the contact. Bjorkland [1997] and Eriten *et al.* [2011] combined the asperity model of Greenwood and Williamson [1966] with Mindlins treatment of the tangential contact problem to define a statistical estimate of the resulting dissipation, a similar approach was used by Bureau *et al.* [2003] to interpret the results of experimental dissipation measurements under microslip conditions. In previous works, the authors proposed, also similar approaches with models and experimental correlations to take into account the energy losses in the contact. A rheological contact model based on the extended Greenwood model with micro-contacts and statistical distributions was developed and studied. Experimental results and simulations are compared in order to assess and discuss the model, [Bouchaala *et al.*, 2013, 2014].

The geometrical uncertainties have an important effect on the loss factor and the stiffness of the structure. To minimize the uncertainties on simulations results, we can minimize the geometrical uncertainties by geometrical specifications of the roughness. But this solution strongly depends on the statistical distribution of the roughness, if robust results is expected, it could be possible to define an geometry

with lesser influence on results. In this work, only the geometrical defects taken into account are of 1st and 2nd (order standards [NF EN ISO 4287-4288, 1998] and [NF EN ISO 12085, 1998]), form defects and waviness defects. The purpose of this study is to find a simple model with a quite good correlation to the experimentation. This, to be able to propose which kind of defect is possible to produce to reach a given level of damping. First, the aim is to compute the real contact zones and the real pressure field in the joints. Second, to calculate the energy losses, the tangential behavior is introduced. This is done thanks to Mindlin's model. Finally, the model is generalized to a multi-contact interface.

2. Model of the Interface

In order to model the contact of a real surface, a multiple spherical contact model, based on Hertz' and Mindlin's theories, is proposed.

2.1. *Parameters of multiple spherical contact model*

The geometrical defects can be described as the members of a statistical population. The experimental observations (Fig. 8) show that the zones in contact can be considered as spheres and their population can be divided into two families, see Fig. 3:

- G-Spheres, the largest, that ensure the rigidity of the interface. They are the first to come into contact during the normal loading. They might not slide completely, thus they are only in partial sliding.
- P-Spheres, the smallest. They are the last to come into contact. They might slide partially or completely.

The interface loading is characterized by the normal displacement δ_n of the two normal planes constituting the interface. Before the loading, the difference between

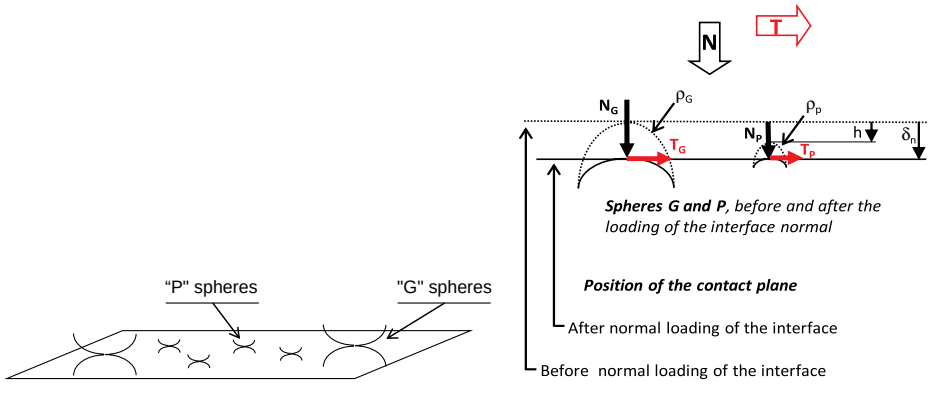

Fig. 3. Left: Simplified description of the population of geometrical defects. Right: Balance between local and global forces.

the heights of the two families of spheres is called h. There are m G-spheres of radius ρ_G and n P-spheres of radius ρ_P. Figure 3, on the right, describes the balance between the global normal load N, the tangential load T and the distribution of local normal and tangential forces N_P, T_P, N_G, T_G of both families of asperity.

$$\begin{aligned} N &= mN_G + nN_P \\ T &= mT_G + nT_P \end{aligned} \tag{1}$$

2.2. *Physical model for one asperity*

The distribution of the normal load N is a function of the normal displacement δ_n and is defined, for a single spherical contact, by Hertz' theory [Hertz, 1881] as follows:

$$\delta_n = \frac{1}{\rho}\left(\frac{3N\rho}{4E^*}\right)^{\frac{2}{3}} \tag{2}$$

with $\frac{1}{E^*} = \frac{1-\nu_1^2}{E_1} + \frac{1-\nu_2^2}{E_2}$ and $\frac{1}{\rho} = \frac{1}{R_1} + \frac{1}{R_2}$,
where E_i, ν_i and R_i are respectively the modulus of elasticity, the poisson's ratio and the radius of curvature of the two solids in contact.

Once the normal load N is applied, a tangential displacement δ is applied between the two surfaces in contact, see Fig. 4. The Mindlin theory [Mindlin, 1949; Mindlin *et al.*, 1952], gives the expression of the displacement induced by partial sliding of the contact surface, as

$$\delta = \frac{3\mu N}{16} G^* \frac{a^2 - c^2}{a^3} \tag{3}$$

with $G^* = \frac{2-\nu_1^2}{G_1} + \frac{2-\nu_2^2}{G_2}$ and $G_j = \frac{E_j}{2(1+\nu_j)}$

From the previous equations, Johnson [1987] offers the solution for a spherical contact, initially loaded with a constant normal load N, and then subjected to a tangential load T oscillating between $\pm T_{\max}$ with $T_{\max} < \mu N$, see Fig. 5. This loading

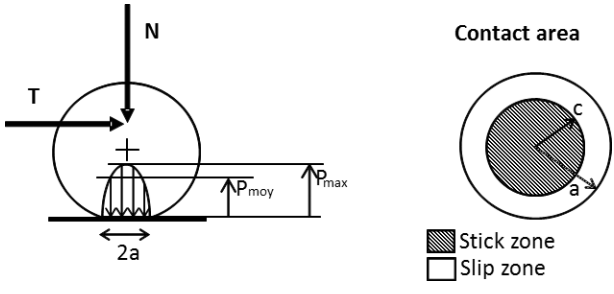

Fig. 4. Schematic elastic spheres pressed by a constant normal force N and subjected to an oscillating tangential force T.

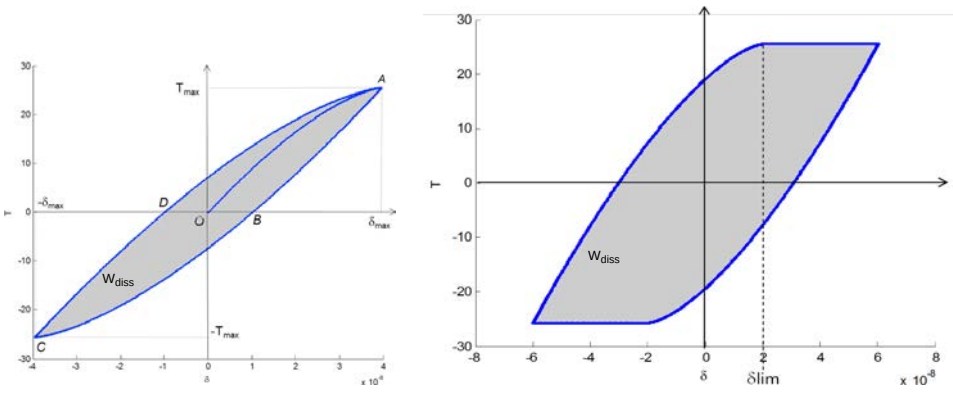

Fig. 5. Left: Loading cycle with partial slip for one spherical contact. Tangential load $T(N)$ versus δ displacement in the contact (m). Right: Loading cycle with macro-slip for one spherical contact. Tangential load $T(N)$ versus δ (m) displacement in the contact.

is divided into three phases:

- Phase 0, curve OA: initial tangential loading, $T \in [0 \quad T_{\max}]$

$$\delta = \frac{\mu N}{16a} G^* \left[1 - \left(1 - \frac{T}{\mu N} \right)^{\frac{2}{3}} \right] \tag{4}$$

- Phase 1, curve ABC: cycle tangential unloading, $T \in [T_{\max} \quad -T_{\max}]$

$$\delta = \frac{\mu N}{16a} G^* \left[2\left(1 - \frac{T_{\max} - T}{2\mu N} \right)^{\frac{2}{3}} - \left(1 - \frac{T_{\max}}{\mu N} \right)^{\frac{2}{3}} - 1 \right] \tag{5}$$

- Phase 2, curve CDA: cycle tangential loading, $T \in [-T_{\max} \quad T_{\max}]$

$$\delta = \frac{\mu N}{16a} G^* \left[-2\left(1 - \frac{T_{\max} + T}{2\mu N} \right)^{\frac{2}{3}} + \left(1 - \frac{T_{\max}}{\mu N} \right)^{\frac{2}{3}} + 1 \right] \tag{6}$$

The area defined by the cycle gives the dissipated energy for a cycle (5).

$$W_{diss} = \oint T d\delta \tag{7}$$

This energy can be expressed as a function of the tangential displacement δ:

$$W_{diss} = \frac{9\mu^2 N^2}{10a} G^* \left[1 - \left(1 - \frac{\delta}{\delta_{\lim}} \right)^{\frac{5}{2}} - \frac{5}{6} \left(1 - \left(1 - \frac{\delta}{\delta_{\lim}} \right)^{\frac{3}{2}} \right) \left(2 - \frac{\delta}{\delta_{\lim}} \right) \right] \tag{8}$$

where $\delta_{\lim} = \frac{3\mu N G^*}{16a}$ defines a limit value of tangential displacement for each type of spherical contact for which there is the passage from the macro-slip phase to the total-slip one, see Mindlin's theory [Mindlin, 1949; Mindlin *et al.*, 1952]. This limit is defined on a loading cycle including macro-slip, see Fig. 5.

2.3. *Physical model for multiple contacts*

Using the force relations given in Eq. (1) and the Hertz' model of Eq. (2), the normal load on the interface constituted with several contacts can be expressed as:

$$N = \frac{4}{3}E^* \left[m\rho_G^{\frac{1}{2}}\delta_n^{\frac{3}{2}} + n\rho_P^{\frac{1}{2}}(\delta_n - h)^{\frac{3}{2}} \right] \tag{9}$$

if $\delta_n - h > 0$ otherwise

$$N = \frac{4}{3}E^* \left[m\rho_G^{\frac{1}{2}}\delta_n^{\frac{3}{2}} \right] \tag{10}$$

In the following, we are going to consider the case with both P-Spheres and G-Spheres in contact, see Eq. (9). Once the normal load is applied, a tangential displacement δ is then imposed. The latter is assumed to be the same for every spherical contact. According to the value of δ, three phases can be highlighted, see Fig. 6:

- "Generalized partial slip" (GPS): G- and P-spheres do not slip totally.
- "Pseudo-partial slip" (PPS) : G-spheres remain in partial slip and P-spheres slip totally.
- "Total slip" (TS) : G- and P-spheres slip totally.

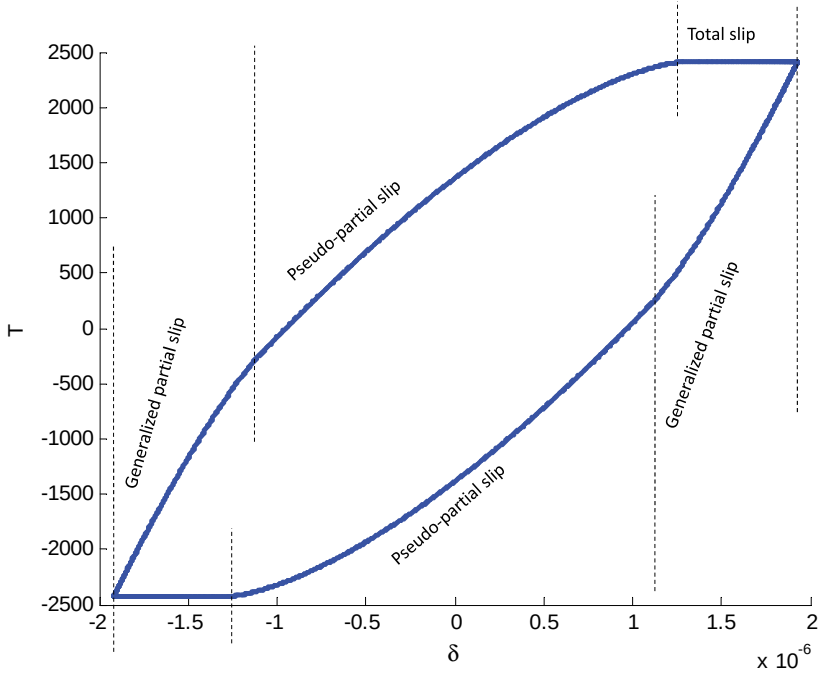

Fig. 6. Loading cycle for multiple contacts model. Tangential load $T(N)$ versus δ (m) displacement in the contact.

The distribution of the tangential load is function of the normal displacement δ_n:

- For the phase of generalized-partial slip (GPS)

$$T = m\mu N_G \left[1 - \left(1 - \frac{\delta}{\delta_{G\,\mathrm{lim}}}\right)^{\frac{3}{2}}\right] + n\mu N_P \left[1 - \left(1 - \frac{\delta}{\delta_{P\,\mathrm{lim}}}\right)^{\frac{3}{2}}\right] \tag{11}$$

- For the phase of pseudo-partial slip (PPS)

$$T = m\mu N_G \left[1 - \left(1 - \frac{\delta}{\delta_{G\,\mathrm{lim}}}\right)^{\frac{3}{2}}\right] + n\mu N_P \tag{12}$$

The loading cycle of the multiple spherical contacts is plotted in Fig. 6. The comparison of the later with the shape of the cycles given by a single spherical contact, of Fig. 5, shows a new behavior during the loading especially when the P-Spheres begin to slip completely.

Equation (7), which defines the energy dissipated by a single spherical contact, with Eqs. (11) and (12), are used to define the energy dissipated by a multiple spherical contact:

$$W_{diss} = \frac{9\mu^2}{10} G^* (w_G + w_P) \tag{13}$$

where w_G is always in partial-slip

$$w_G = m\frac{N_G^2}{a_G}\left[1 - \left(1 - \frac{\delta}{\delta_{G\,\mathrm{lim}}}\right)^{\frac{5}{2}} - \frac{5}{6}\left(1 - \left(1 - \frac{\delta}{\delta_{G\,\mathrm{lim}}}\right)^{\frac{3}{2}}\right)\left(2 - \frac{\delta}{\delta_{G\,\mathrm{lim}}}\right)\right] \tag{14}$$

and w_P is defined according to the phase:
in generalized partial slip (GPS):

$$w_P = n\frac{N_P^2}{a_P}\left[1 - \left(1 - \frac{\delta}{\delta_{P\,\mathrm{lim}}}\right)^{\frac{5}{2}} - \frac{5}{6}\left(1 - \left(1 - \frac{\delta}{\delta_{P\,\mathrm{lim}}}\right)^{\frac{3}{2}}\right)\left(2 - \frac{\delta}{\delta_{P\,\mathrm{lim}}}\right)\right] \tag{15}$$

in pseudo-partial slip (PPS):

$$w_P = \mu N_P \delta \tag{16}$$

2.4. *Analysis of the model parameters influence*

It is interesting to analyze the evolution of the friction-induced vibration-damping through the loss-factor η. The mathematical definition of the loss factor is

$$\eta = \frac{W_{diss}}{2\pi W_{ext}} \tag{17}$$

where W_{diss} is the disipated energy in the interface and W_{ext} is the work of external forces. The loss-factor is a function of the multiple-contact model parameters. The values of these parameters can be debatable: the number of P and G-spheres depends on the manufacturing process, the friction coefficient can change during

Table 1. Parametric study: Values of the parameters.

m	n	$N(N)$	$\delta_n(10^{-7}m)$	$h(10^{-7}m)$	μ	Figure
5	18	460	2.5	2.4	0.2	7a (Ref)
5	4, 9	450, 454	2.5	2.4	0.2	7b
	36, 72	474, 501				
1, 3	18	103, 282	2.5	2.4	0.2	7c
8, 11		728, 997				
5	18	572, 710	2.7, 2.9	2.4	0.2	7d
		869	3.1			
3, 5	18	250, 460	2.3, 2.5	2.2, 2.4	0.2	7e
7		716	2.7	2.6		
5	18	460	2.5	2.4	0.15, 0.18	7f
					0.25, 0.3	

the vibration motion according to wear, temperature, etc. In order to visualize the effects of each parameter, a study of the sensibility of the parameters has been carried out, see Table 1. The results have been summarized in Fig. 7 and discussed in the following section.

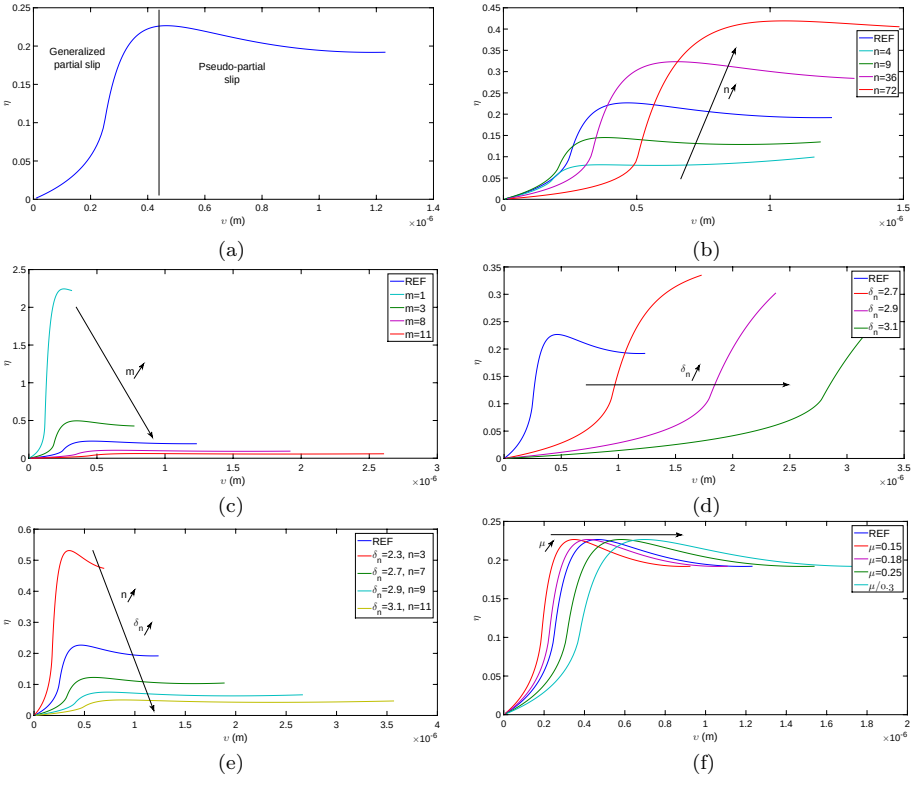

Fig. 7. Results of the parametric study.

As said in Sec. 2.1, the model contains only two kinds of spheres, under the assumption that the G-spheres provide the rigidity of the interface and remain in partial slip whereas the P-spheres slip totally when δ becomes large enough. The identification of the contacts can be tricky. For the studied specimen, Sec. 3 gives the characteristics of the surfaces : 5 G-spheres and 18 P-spheres can be considered from the measurements. The other parameters are chosen from our knowledge, see line 1 of Table 1. This set of parameters provides the reference case which will be shown on Fig. 7. On X-axis, the displacement v at the center of the beam is plotted, while on Y-axis the loss factor η is shown.

The first design parameters of the parametric study are n and m, respectively the number of P-spheres and G-spheres. As n increases, the maximum damping also increases, however the vibration amplitude v has to be greater, as it can be seen in Fig. 7(b). On the contrary, see Fig. 7(c), when m increases, the damping decreases: this is due to the fact that δ_n is fixed, which implies that the global normal load, increases when m increases. The number of G-spheres for a given δ_n directly influences the resultant normal load and the tangential stiffness of the interface. If δ_n increases, as h is fixed, the compression of the P-spheres no longer allows the phase of macro-slip: this implies that the damping increases for greatest the values of v, see Fig. 7(d).

In fact, the parameters are not independent, when the normal displacement increases, P-spheres are more compressed and therefore they have the same behavior than G-spheres: no phase of macro-slip. However others spheres, previously not in contact, find themselves slightly compressed and dissipate energy by macro-slip. So increasing the normal displacement leads to an increase of the number m of G-spheres. Figure 7(e) presents the evolution of the loss factor, increasing both the normal displacement δ_n and the number m of G-spheres. While the number of P-spheres n remains constant, see Table 1. The damping function remains slightly dependent on the amplitude. To conclude this analysis, it is interesting to consider the effect of a variation of the friction coefficient μ. This leads to an evolution of the threshold of macro-slip for the P-spheres, see Fig. 7(f).

3. Experimental Characterization of the Joint Surfaces of the Test Bench

In order to obtain the real contact surfaces, 3D measurements were made, with a ZEISS OI 442 machine, see Fig. 8. On each surface, a million points were measured. After filtering and re-sampling, a mesh constituted by 1200×800 pixels has been obtained. The contact takes place at the highest points over the imaginary perfect plane. To choose a cloud of points, defining the contact-area, only the "higher" points, 10% of the set of points, were retained. Figure 8 shows that the surfaces present irregularities on which contacts. To determine the influence of the defects on the vibration-damping, the surface irregularities are modeled as sphere caps, see Fig. 9, where df and $\emptyset(m)$ are respectively the height and the diameter of the

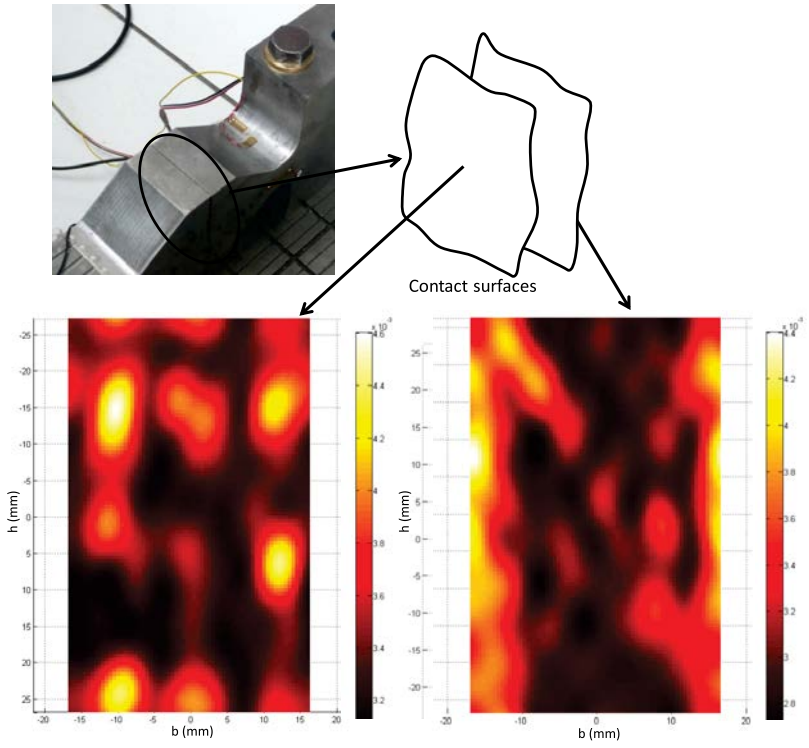

Fig. 8. 3D measurements of test-bench interfaces (in mm) from ZEISS OI442.

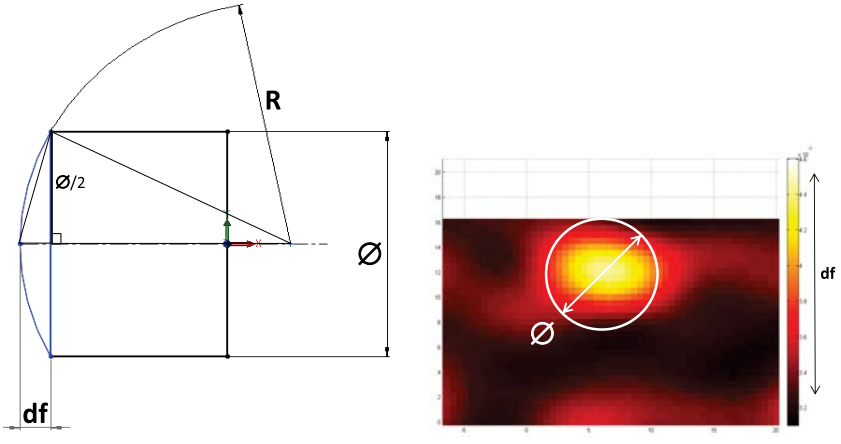

Fig. 9. Left: geometric modeling of the sphere. Right: identification of a spherical contact parameters from the measurement.

Table 2. Model parameters.

Spheres	Number	$df(m)$	$\emptyset(m)$	$R(m)$
G	$n = 5$	$1.7\ 10^{-6}$	$1.7\ 10^{-2}$	23.8
P	$m = 18$	$1.2\ 10^{-6}$	$1.6\ 10^{-2}$	26.7
h		$2.4\ 10^{-7}m$		

sphere cap. R, the radius of curvature is calculated from df and $\emptyset$ using the following expression:

$$R = \frac{\frac{\emptyset^2}{4} + df^2}{2df} \tag{18}$$

In accordance with the model, two types of spheres are identified on each surface, see Table 2. Following a classical assumption, see Greenwood and Williamson [1966] and Greenwood and Wu [2001], in a contact between two surfaces, one is considered to be flat, while the other one includes all the defects. The numbers $m = 5$ and $n = 18$ have been evaluated by counting the number of defects of both sides of the interface. There are 5 that belong to the big defects category and 18 that belong to the small defect category.

Thus, during the normal loading of the interface, the G-spheres ensure the rigidity of the interface and are the first and most compressed, whereas the P-spheres are only slightly compressed.

4. Numerical Simulation of the Test Bench

The energy dissipated is plotted in Fig. 10. As function of the displacement δ, i.e., Eq. (13), the figure shows three behaviours: for small displacements W_{diss} is nil; for intermediate displacements W_{diss} is governed by Eq. (15) of the GPS and for high displacements W_{diss} is governed by Eq. (16) of the PPS. Overall, W_{diss} is governed by a non-continuous polynomial function with an exponent between 0 and 2. Taking into account the external force applied on the structure to obtain the dynamic behavior, it is possible to define the loss factor of the structure:

$$\eta = \frac{W_{diss}}{2\pi W_{ext}} \tag{19}$$

where the work of external forces W_{ext} can be expressed as function of the displacement at the center of the beam υ:

$$W_{ext} = \frac{1}{2} K_m \upsilon^2 \tag{20}$$

W_{ext} is governed by a quadratic function. Thus the loss-factor is first nil due to W_{diss}, then it increases and it tends to zero when δ tends to infinite, see Fig. 7(a). The latter is plotted for a 460 N pre-load and for the data summarized in Table 1. The transition from GPS to PPS leads to a drastic change in the evolution of the loss

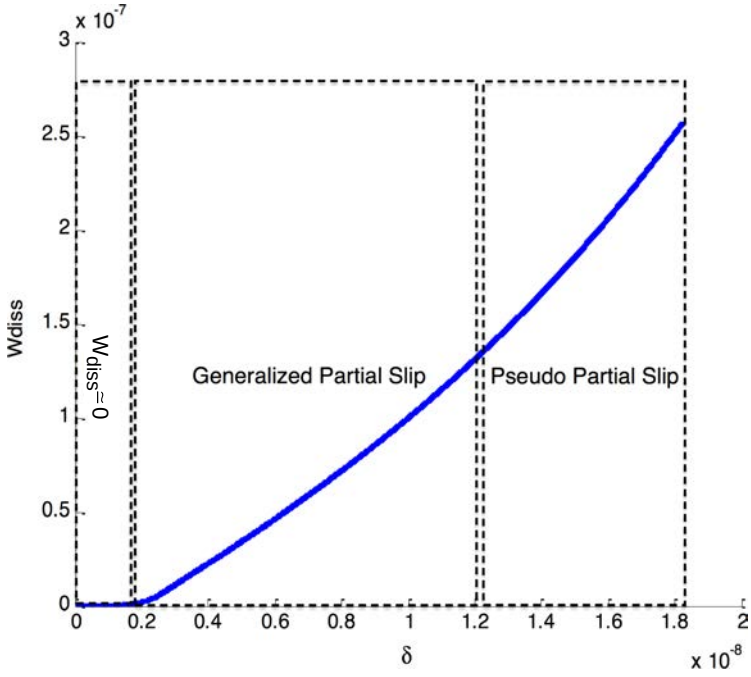

Fig. 10. Energy dissipated for a multi-contact interface. $W_{diss}(J)$ versus displacement $\delta(m)$.

factor. To compare the experimental results with the results provided by the model, one needs to isolate the contribution of interfaces studied from the other sources of damping. The two structures, assembly and monolithic, have the same geometry and the same boundary conditions, it is thus possible to consider two distinct sources of damping. We distinguish the dissipation induced by the interfaces (friction joints) f_{d2} from the dissipation provided by all the others sources f_{d1} (clamps, intrinsic damping of the material, etc.):

$$m\ddot{v} + kv = f_{d1}(\dot{v}, v) + f_{d2}(\dot{v}, v) \tag{21}$$

Thus, the dissipated energy can be written as

$$W_{diss} = \oint (f_{d1}(\dot{v}, v) + f_{d2}(\dot{v}, v))dv \tag{22}$$

Both energies are separable by subtraction. It is considered that W_{d1} can be identified by a test on the monolithic beam and W_{d2} can be calculated by subtracting the damping rate of the monolithic beam (see Fig. 11). The results of the simulations, with plane surfaces in interfaces [Peyret *et al.*, 2010] and with two types of defects in interfaces, are positioned at the intrinsic damping of the assembly besause this contribution are not taken into account in these models. It is possible to compare models simulation to the experimental results [Dion *et al.*, 2013]. This comparison of the experimental results with those given by the model highlights a better

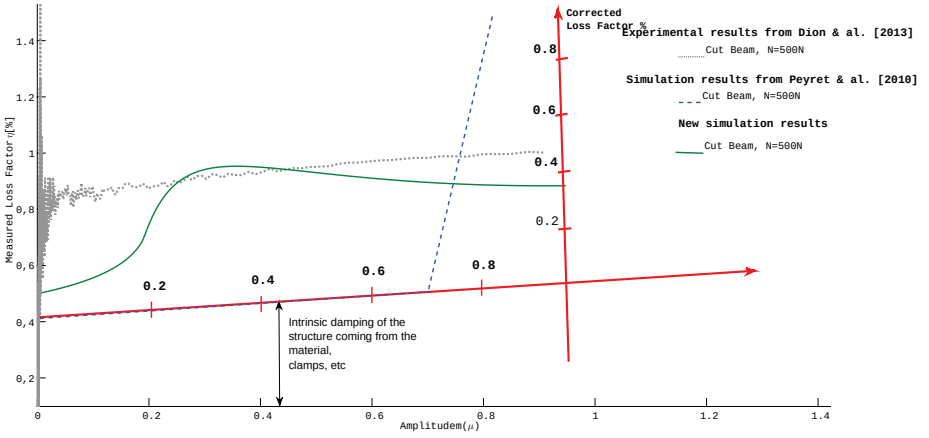

Fig. 11. Comparison between experimental results, simulation results obtained under perfectly flat surfaces assumption and simulation results obtained taking under account surface defects.

agreement than in Peyret *et al.* [2010]. Taking into account geometrical defaults in interfaces, even if the parameters of the retained geometry for model is quite simple, it allows a good agreement. The choosen model has a good agreement with experimental results, except for small amplitudes. This difference is probably due to the assumption considering only two types of spheres of different heights. In fact this model does not take into account the progressivity of the spheres height in the interfaces and the fact that the irregularities of the surface outcrop the contact and dissipate some energy at small vibration amplitudes.

5. Conclusion

Unlike models that take into account the interface as a geometrically perfect plane [Peyret *et al.*, 2010], taking into account form and waviness defects of the surface allows to evaluate damping at the interfaces also at the smallest vibration amplitudes. A model that takes into account form and waviness surface defects was developed in order to model the evolution of damping as a function of strain amplitude. This new approach is a multi-spherical contact modeling of the interface, based on the behavior of a single spherical contact developed by Hertz and Mindlin. This multi-scale model considers the presence of two types of contacts: contacts which ensure the rigidity of the interface and contacts which dissipate energy. This modeling allows to obtain a better correlation between the simulation results and the experimental measurements. Further work aims to link macro-models used for vibration analysis [Quinn, 2012], with local parameters. According to the function of the studied assembly, this work allows to design contact surfaces. In order to design a stiff assembly, the model can be used to define the maximum admissible surface defect. On the contrary, in order to design a dissipative assembly, the model can be used to define controlled or desired surface defects.

Appendix A Nomenclature

Symbol	Description	Units
a	Radius of the contact	m
A_0	Nominal contact area	m^2
A_R	Real contact area	m^2
c	Radius of the sticking zone	m
d_f	Height of the spheres	m
E^*	Composite modulus of elasticity	N/m^2
G^*	Inverse composite shear modulus	m^2/N
$G-spheres$	First type of sphere	
h	Height difference between the two types of spheres	m
K_{mcis}	Shear modal stiffness	N/m
K_m	Modal Stiffness	N/m
m	Number of G-spheres	
n	Number of P-spheres	
N	Normal load	N
N_i	Local normal load	N
p_R	Real contact pressure	N/m^2
$P-spheres$	Second type of sphere	
T	Tangential load	N
T_i	Local tangential load	N
W_{diss}	Energy dissipation	J
W_{ext}	External works	J
δ	Tangential displacement	m
δ_n	Normal displacement	m
δ_{ilim}	Limit of partial sliding	m
ξ	Damping	%
η	Loss factor	%
μ	Coefficient of friction	
ρ	Composite radius of curvature	m
υ	Displacement at the center of the structure	m
ν	Poisson's ratio	
$\emptyset$	Diameter of the apparent surface	m

Appendix B Design of the Experimental Device

The principle of the experimental device Fig. 1 was justified in previous works, see [Dion *et al.*, 2013] and [Peyret *et al.*, 2010]: it is a clamped-clamped beam excited on its first bending mode. The beam is built up with three parts linked by two planar joints. A normal pre-load N is applied on both extremities of the beam before there

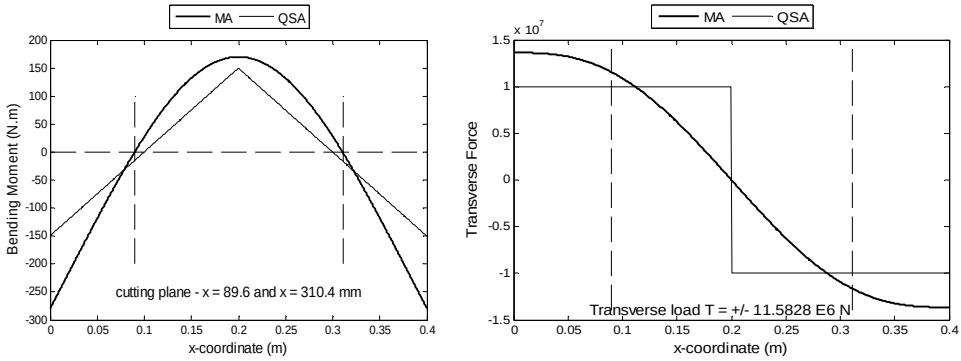

Fig. B.1. Bending moment (left) and transverse force (right) belonging to the cross sections of the beam studied. The dashed lines indicate the cutting planes located at $x = 100$ and 300 mm under the quasi static assumption and at $x = 89.6$ mm and 310.4 mm under the modal assumption. These results were obtained considering a analytical beam model under a Timoshenko assumption.

are clamped to the ground. The three parts remain in contact even during the bending motion due to the normal pre-load N and the friction between the counter-parts. This design allows avoiding coupling between pre-load induced normal stresses in the planar joints and the vibration-induced shear stresses due to the zero bending moment at the location of the joints, see Fig. B.1. In the previous paper (see [Peyret *et al.*, 2010]), the beam was studied under a quasi-static assumption (QSA), i.e., the normal and shear stresses were computed using the definition of the static bending moment when the beam was loaded with a centered transverse load. A more recent work (see [Dion *et al.*, 2013]) showed that QSA leads to errors in defining the zero-bending-moment section and for the amplitude of the transverse load in this section. By using the definition of the first bending mode (MA), the bending moment is equal to zero in the cross sections located at x = 89.6% of $L/4$, see Fig. B.1. Moreover the transverse load is 20% higher for MA than for QSA. By improving the shape of the beam, it is possible to define the position of the cutting section which leads to a zero bending moment. This section has to be well placed even if the experimental mode shape is slightly different from the theoretical one due to machining errors. The constant section over the length of the beam does not allow obtaining this robustness. The difference between MA and QSA illustrates this lack of robustness in the design well.

The beam has to be as thick as possible in order to maximize the damping of the structure. Machining errors can lead to badly positioned cutting-sections and therefore to coupling between the normal load and the vibration motion. In order to ensure robustness in the face of machining errors, the authors propose a design that allows obtaining a nil bending moment over a non-zero length Fig. B.2. In order to obtain uniformly distributed normal stress over the cutting plane, the thickness of the beam changes smoothly over its length. Finally, particular attention was given

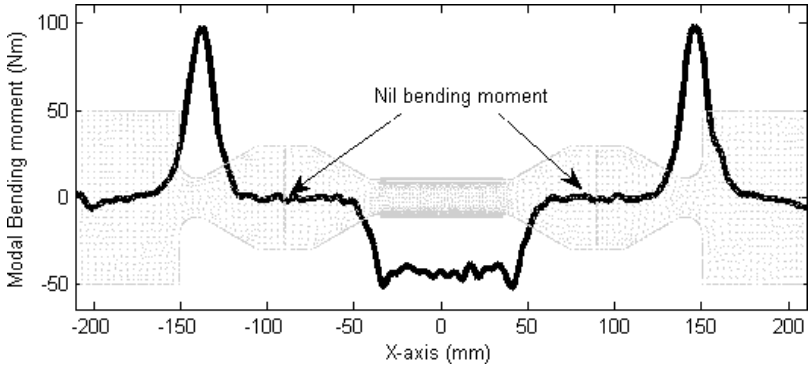

Fig. B.2. Bending moment plotted over the beam length. Particular attention should be given to the width of the zero moment zone which makes the device robust to machining errors.

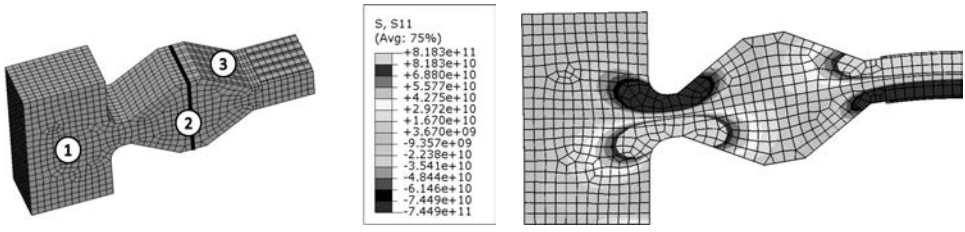

Fig. B.3. Left: New design, 3D view of half of the beam. The clamp is located on Vol. 1. Volume 2 is cut in order to make the joint. Volume 3 has been designed to ensure the normal stresses are uniformly distributed. Right: Normal stress distribution under the first mode shaped prescribed displacement. The normal stresses are zero in the neighborhood of the cutting plane.

to obtaining the highest frequency for the second bending mode in order to avoid coupling between the first two modes. All these design constraints led the authors to define the geometry of the Fig. B.3: the plane of the beam is symmetrical; it has two clamped blocks and two interface areas . The blocks around the two interface zones are designed to maximize the width of the zone where the bending moment is nil, see Fig. B.2.

References

Ahmadian, H. and Jalali, H. [2007] "Identification of bolted lap joints parameters in assembled structures," *Mechanical Systems and Signal Processing* **21**(2), 1041–1050.

Beards, C. F. and Williams, J. L. [1977] "The damping of structural vibration by rotational slip in joints," *Journal of Sound and Vibration* **53**(3), 333–340.

Berthillier, M., Dupont, C., Mondal, R. and Barrau, J. J. [1998] "Blades forced response analysis with friction dampers," *Journal of Vibration and Acoustics* **120**(2), 468–474.

Bjorkland, S. [1997] "A random model for micro-slip between nominally flat surfaces," *ASME Journal of Tribology* **119**, 726–732.

Bouchaala, N., Dion, J.-L., Peyret, N. and Haddar, M. [2013] "Micro-slip induced damping in the contact of nominally flat surface," *International Journal of Applied Mechanics* **05**(1), 81–93.

Bouchaala, N., Peyret, N., Tawfiq, I., Dion, J.-L. and Haddar, M. [2013] "Compact model and identification process for friction induced damping in a rotational joint with flawed surfaces," *International Journal of Solids and Structures* **51**(21–22), 3570–3578.

Bureau, L., Caroli, C. and Baumberger, T. [2003] "Elasticity and onset of frictional dissipation at a non-sliding multi-contact interface," *Proceedings of the Royal Society A* **459**, 2787–2805.

Chevallier, G., Macewko, F. and Robbe-Valloire, F. [2003] "Dynamic friction evolution during transient sliding," *Tribology Series* **43**, 537–543.

Dion, J.-L., Chevallier, G. and Peyret, N. [2013] "Improvement of measurement techniques for damping induced by micro-sliding," *Mechanical Systems and Signal Processing* **34**(1), 106–115.

Dion, J.-L., Chevallier, G., Penas, O. and Renaud, F. [2013] "A new multicontact tribometer for deterministic dynamic friction identification," *Wear* **34**(1), 106–115.

Eriten, M., Polycarpou, A. A. and Bergman, L. A. [2011] "Surface roughness effects on energy dissipation in fretting contact of nominally flat surfaces," *ASME Journal of Applied Mechanics* **78**.

Esteban, J. and Rogers, C. A. [2000] "Energy dissipation through joints: Theory and experiments," *Computers & Structures* **75**(4), 347–359.

Goodman, L. E. and Klumpp, J. H. [1993] "Analysis of slip damping with reference to turbine blade vibration," *ASME Applied Mechanics Division* **23**(3), 421–429.

Goryacheva, I. G. and Dobychin, M. N. [1991] "Multiple contact model in the problems of tribomechanics," *Tribology International* **24**(1), 29–35.

Goyder, H., Ind, P. and Brown, D. [2009] "Development of a method for measuring damping in bolted joints," *Proceedings of IDTEC ASME*.

Greenwood, J. A. and Tripp, J. H. [1970] "The contact of two nominally flat rough surfaces," *Proceedings of the Institution of Mechanical Engineers* **185**(1), 625–633.

Greenwood, J. A. and Williamson, J. B. P. [1966] "Energy dissipation through joints: Theory and experiments," *Proceedings of the Royal Society of London. Series A. Mathematical and Physical Sciences* **295**(1442), 300–319.

Greenwood, J. A. and Wu, J. J. [2001] "Surface roughness and contact: An apology," *Meccanica* **36**(6), 617–630.

Heller, L., Foltete, E. and Piranda, J. [2009] "Experimental identification of nonlinear dynamic properties of built-up structures," *Journal of Sound and Vibration* **327**(1), 183–196.

Hertz, H. [1881] "On the contact of elastic solids," *Journal fur die Reine und Andgewandte Mathematik* **92**(110), 156–171.

Johnson, K. L. [1987] *Contact Mechanics* (Cambridge University Press).

Korkmaz, I., Barrau, J. J., Berthillier, M. and Creze, S. [1993] "Analyse dynamique expérimentale d'une poutre amortie par un amortisseur à frottement sec," *Mécanique industrielle et matériaux* **46**(3), 145–149.

McCool, J. I. [1985] "Predicting microfracture in ceramics via a microcontact model," SKF Engineering and Research, King of Prussia, PA (USA).

Metherell, A. F. and Diller, S. V. [1968] "Instantaneous energy dissipation rate in a lap joint — uniform clamping pressure," *Journal of Applied Mechanics* **35**, 123–128.

Mindlin, R. D. [1949] "Compliance of elastic bodies in contact," *ASME Journal of Applied Mechanics* **16**, 259–268.

Mindlin, R. D., Mason, W. P., Osmer, T. F. and Deresiewicz, H. [1952] "Effects of an oscillating tangential force on the contact surfaces of elastic spheres," *Proceedings of the First US National Congress of Applied Mechanics*, pp. 203–208.

NF EN ISO 12085 [1998] "Spécification géométrique des produits (GPS) - état de surface : Méthode du profil — Paramètres liés aux motifs" .

NF EN ISO 4287-4288 [1998] "Spécification Géométrique des Produits (GPS) Etat de surface : Méthode du Profil Règles et procédures pour l'évaluation de l'état de surface".

Peyret, N., Dion, J.-L., Chevallier, G. and Argoul, P. [2009] "Nonlinear dynamic behavior modelling of a planar friction interface in a structure assembly," *Proceedings of IDTEC ASME*.

Peyret, N., Dion, J.-L., Chevallier, G. and Argoul, G. [2010] "Micro-slip induced damping in planar contact under constant and uniform normal stress," *International Journal of Applied Mechanics* **02**(2), 281–304.

Peyret, N., Chevallier, G. and Dion, J.-L. [2011] "Energy dissipation by micro-slip in an assembly, analytic and experimental approach," *Proceedings of IDTEC ASME*.

Pian, T. H. H. [1957] "Structural damping of a simple built-up beam with riveted joints in bending," *ASME Journal of Applied Mechanics* **24**, 35–38.

Poudou, O. [2007] "Modeling and analysis of the dynamics of dry-friction-damped structural systems," Ph.D. thesis, University of Michigan.

Pugliese, G., Tavares, S. M. O., Ciulli, E. and Ferreira, L. A. [2008] "Rough contacts between actual engineering surfaces: Part II. Contact mechanics," *Wear* **264**(11), 1116–1128.

Quinn, D. D. [2012] "Modal analysis of jointed structures," *ASME Journal of Applied Mechanics* **331**(1), 81–93.

Segalman, D. J. [2010] "A modal approach to modeling spatially distributed vibration energy dissipation," Technical Report SAND2010–4763, Sandia National Laboratories.

Tsukizoe, T. and Hisakado, T. [1965] "On the mechanism of contact between metal surfaces: The penetrating depth and the average clearance," *Journal of Basic Engineering* **87**(3), 666–672.

Ungar, E. E. [1973] "The status of engineering knowledge concerning the damping of built-up structures," *Journal of Sound and Vibration* **26**(1), 141–154.

Whiteman, W. E. and Ferri, A. A. [1996] "Displacement-dependent dry friction damping of a beam-like structure," *Journal of Sound and Vibration* **198**(3), 313–329.